Materials Advances

PAPER

Check for updates

Near-infrared luminescence and high thermal stability of Rb2NaScF6:Cr3+ phosphor for spectroscopy applications†

Lingxiang Chu, Yi Qin, Tao Yang, Jing Wan, Qiang Zhou, [ID] * Huaijun Tang, [ID] Yanqing Ye and Zhengliang Wang [ID] *

The search for chromium-doped near-infrared phosphor for spectroscopy application has attracted widespread concern. Herein, we prepared a double-perovskite fluoride phosphor, $Rb_2NaScF_6:Cr^{3+}$ (abbreviated as RNSF:Cr), with wide blue excitation and near-infrared emission bands using a co-precipitation method. The crystal and electronic structures, as well as the luminescent properties were systematically investigated. Evidences show that RNSF offers a weak coordination environment and a wide bandgap for Cr^{3+} doping. By virtue of the weak electron–phonon coupling effect and the large activation energy, a high photoluminescence thermal stability was observed at 150 °C, with a ratio of 92% of that at 25 °C. In view of the high thermal stability, RNSF:Cr phosphor was incorporated into phosphor-converted light-emitting diodes to evaluate its potential use for near-infrared spectroscopy applications.

Introduction

As an up-and-coming analytical technique, near-infrared (NIR) spectroscopy plays a crucial role in multifunctional application fields of night vision, food inspection and non-contact biomedical imaging owing to the invisibility, strong penetration and non-destruction benign natures of NIR light.[1–3] Nowadays, phosphor-converted light-emitting diode (pc-LED) consisting of NIR phosphor with a blue LED chip that offers the benefits of high efficiency, compactness and long lifetime is considered to be the most popular technical solution to emit NIR light and realize portable and real-time detection of product quality and human health.[4,5] Considering the vital role of colour conversion in pc-LED device, NIR phosphor with customized spectral features of blue excitation and NIR emission is critically important.[6]

A series of luminescent activators, *i.e.*, Eu^{2+}, Fe^{3+}, Mn^{4+} and Cr^{3+}, have been utilized one after another to generate NIR emission.[7–10] Considering the spectral adaption with commercial

*Key Laboratory of Green Chemistry Materials in University of Yunnan Province, Key Laboratory of Advanced Synthetic Chemistry (Yunnan Minzu University) of National Ethnic Affairs Commission, School of Chemistry and Environment, Yunnan Minzu University, Kunming 650500, P. R. China.
E-mail: q-zhou@ymu.edu.cn, wangzhengliang@foxmail.com*

† Electronic supplementary information (ESI) available: Details to the SEM and elemental mapping images, EPR spectrum, TG curve, and crystallographic parameters after Cr^{3+} doping. NIR output power and photoelectric conversion efficiency of LED device, and some typical Cr^{3+}-doped fluoride phosphors. See DOI: https://doi.org/10.1039/d3ma00522d

blue LED chip and Mn^{4+} luminescence always locates in red and deep red regions, Cr^{3+} is considered as a preferable choice for the generation of NIR emission.[11] Compared with oxide host, *i.e.*, $Mg_7Ga_2GeO_{12}$ or Li_2MgZrO_4,[12,13] the low phonon energy as well as the weak electron–phonon coupling (EPC) strength of fluoride enables its attraction to produce efficient Cr^{3+}-doped NIR phosphor. To date, Cr^{3+}-doped fluorides have attracted widespread attention. The unique $[Ar]3d^3$ electron configuration and the low phonon energy of fluoride empower the generation of Cr^{3+} *d–d* transition that transfers high-energy blue light to low-energy NIR light in weak crystal field. Until now, a plenty of Cr^{3+}-doped fluoride NIR phosphors have been reported, for instance, Zhou and his colleagues recently prepared a Cr^{3+}-doped K_2LiScF_6 fluoride phosphor through a combination of hydrothermal and cation exchange methods. However, it presents a medium thermal stability (75%@ 150 °C).[14] Liang and his co-workers prepared a novel $LiInF_4:Cr^{3+}$ phosphors with an ultra-large full width at half-maximum (FWHM) of 210 nm for vein imaging through a hydrothermal method, but its luminescence ratio only preserves 27% at 100 °C.[15] It should be noted that photoluminescence (PL) thermal stability is a decisive indicator for evaluating the phosphor's application potential since the high working temperature of LED devices, resulting in the exploration of NIR phosphors with excellent PL thermal stability is of great significance.[16–18] Recently, a series of Cr^{3+}-doped fluorides have been endowed high popularity due to their stable structures that enable the excellent thermal stability of Cr^{3+}. For example, Zhou *et al.* presented a $Cs_2NaAl_3F_{12}:Cr^{3+}$ NIR phosphor with an

outstanding luminescence maintenance ratio of 101% at 150 °C for vein imaging application.[19] Our group also reported a highly thermo-stable $LiMgAlF_6:Cr^{3+}$ far-red-emitting phosphor (93.9%@150 °C) for plant growth lighting.[20] However, despite these successful strides, it was found that some examples of Cr^{3+}-activated fluoride NIR phosphors exhibit relatively low PL thermal stability.[21,22] Therefore, to address this issue, preparing Cr^{3+}-doped fluoride NIR phosphor with high PL thermal stability is still worthy of investigation.

In this work, we prepared a NIR-emitting RNSF:Cr phosphor with high PL thermal stability through a co-precipitation method. The crystal and electronic structures, as well as the luminescent properties of RNSF:Cr were characterized and investigated. Evidences show that RNSF offers a weak crystal field with a wide bandgap (6.838 eV) for Cr^{3+} doping. Benefiting from the weak EPC strength ($S = 1.15$) and large activation energy ($\Delta E = 0.251$ eV), RNSF:Cr exhibits an outstanding thermal stability at 150 °C, with a retention rate of 92% of that at room temperature (RT). Based on this observation, NIR pc-LED devices were prepared and used as radiation sources by coating RNSF:Cr powders on blue LED chips for non-destructive vein imaging and night vision applications. The results indicate that the as-synthesized RNSF:Cr phosphor has promising use in pc-LED device for NIR spectroscopy applications.

Experimental

Materials and preparation

Rubidium carbonate (Rb_2CO_3, AR), sodium fluoride (NaF, AR), scandium oxide (Sc_2O_3, AR), ammonium hydrogen fluoride (NH_4HF_2, AR), chromium nitrate nonahydrate ($Cr(NO_3)_3 \cdot 9H_2O$, AR), HF (40 wt% in H_2O) and absolute ethanol were purchased from Shanghai Aladdin Biochemical Technology Co. Ltd., China to synthesize RNSF:Cr phosphor. All raw materials were used as supplied without any further purification. $(NH_4)_3CrF_6$ was prepared using the reported literature method.[23] RNSF:Cr phosphor was synthesized through a co-precipitation method at RT. To demonstrate this, we describe the synthesis procedure for RNSF:0.03Cr sample as an example. Typically, 2.5 mmol of Sc_2O_3 was weighed and dissolved in 5 mL of HF solution under magnetically stirring to form a homogeneous solution. Next, 5 mmol of Rb_2CO_3, 5 mmol of NaF and 0.15 mmol of $(NH_4)_3CrF_6$ were successively added into the solution under stirring at RT for 8 h. Then, the light green precipitates were collected, washed and centrifuged with absolute ethanol for several times, and finally dried at 80 °C for 6 h to obtain the final RNSF:0.03Cr product for later characterization. Different molar ratios of $(NH_4)_3CrF_6$ and Sc_2O_3 were employed to synthesize a series of RNSF:Cr products with various dopant contents.

The chip-on-board (COB) blue chip (Guhoon Optoelectronics Co., Ltd., China) and the as-obtained NIR phosphor were used to fabricate NIR pc-LED device with mass ratio between the UV structural adhesive (Shenzhen Tegu New Materials Co.,

Ltd., China) and the NIR phosphor of 1 : 1. The LED device was dried at 120 °C for 60 min followed by photoelectric tests.

Characterization and computation

The crystal structure and phase purity of the as-prepared RNSF:Cr sample were characterized using a Bruker D8 Advance X-ray diffractometer (XRD) with Cu Kα radiation ($\lambda = 0.15406$ nm). The operating voltage, current, scanning rate, angular range, and step size were 40 kV, 40 mA, 10° min^{-1}, 10°–70°, and 0.02°, respectively. The powder diffraction data for Rietveld analysis were carried out on the same diffractometer with a scanning rate of 1° min^{-1} and an angular range from 5 to 120°. Electron paramagnetic resonance (EPR) spectrum was collected from a Bruker EMXplus-6/1 spectrometer. The morphology and elemental composition were detected from an FEI Nova NanoSEM 450 scanning electron microscope (SEM) with an energy-dispersive X-ray spectrometer (EDS) attachment. The photoluminescence excitation (PLE) and PL spectra, internal quantum efficiency (IQE), and lifetime were recorded from an Edinburgh FLS1000 fluorescence spectrophotometer with an additional integrating sphere. The diffuse reflectance (DR) spectrum was recorded by a Hitachi UH4150 UV-Vis-NIR spectrophotometer using $BaSO_4$ as a reference. The concentration- and temperature-dependent PL spectra were obtained using an AVANTES Avaspec Mini 2048CL-SHB3 fiber spectrophotometer with a temperature heating attachment for warming up and a 460 nm laser diode as the excitation source. Thermogravimetric (TG) data were acquired by a Netzsch TG 209 F1 under nitrogen atmosphere with a heating rate of 10 °C min^{-1} ranging from 30 to 1000 °C. The electroluminescence spectra of the pc-LEDs were examined by an OHSP-350M LED fast-scan spectrophotometer (Hangzhou Hopoo Light & Color Technology Co., Ltd.). The demonstration images were captured by a Canon XA10E industrial camera loaded with NIR and natural modes. Thermographs of LED device recorded at different driven currents were taken with NIR imaging mode.

The Rietveld XRD refinement was performed on a General Structure Analysis System (GSAS) software. The crystal structure was constructed by using a Visualization for Electronic and Structural Analysis (VESTA Ver. 3.4.4) software. The energy bands and electronic structures were estimated by using a CASTEP module of the Materials Studio package based on density functional theory (DFT).

Results and discussion

Fig. 1a shows the XRD patterns of RNSF:xCr ($x = 0$-0.07) samples with various dopant concentrations, in which all diffraction peaks are well indexed into the standard JCPDS card for the cubic $Fm\bar{3}m$ (225) structure of RNSF (JCPDS No. 24-0970). The intense diffraction peaks and the impurity-free patterns suggest the high degree of crystallinities and the single phases of the as-obtained RNSF:Cr samples, verifying the incorporation of Cr^{3+} ion does not change the cubic structure of RNSF host, even with the highest doping content.[24]
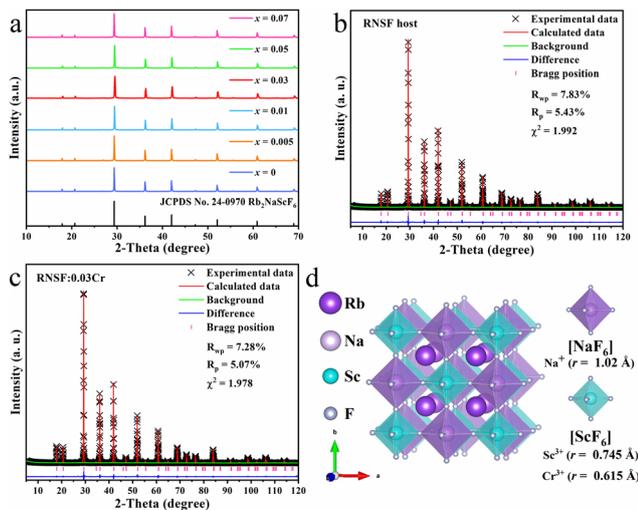
Fig. 1 (a) XRD patterns of RNSF:xCr (x = 0–0.07) samples. (b) and (c) Rietveld refinement results of RNSF host and RNSF:0.03Cr sample. (d) Crystal structure diagram of RNSF host.

Fig. 2 (a) and (b) Band structure, partial and total densities of states of RNSF host. (c) PLE, PL and DR spectra of RNSF:0.03Cr product. (d) Tanabe-Sugano diagram for Cr^{3+} in octahedral symmetry.

Fig. 1b and c exhibit the refined XRD patterns of RNSF host and a selected RNSF:0.03Cr sample, which were carried out on the GSAS program for the purpose of checking the structural difference after Cr^{3+} doping. The satisfactory R_{WP}, R_P, χ^2 factors, that 7.83%, 5.43%, 1.992 for RNSF and 7.28%, 5.07%, 1.978 for RNSF:0.03Cr, suggest that the refinement results are dependable and the crystal structure of RNSF:0.03Cr accords well with RNSF host.[25] The refined lattice parameters of RNSF (a = b = c = 8.6098 Å, V = 638.2544 Å³ and Z = 4) and RNSF:0.03Cr (a = b = c = 8.6085 Å, V = 637.9565 Å³ and Z = 4) are listed in Table S1 in ESI,† further verifying that the RNSF:0.03Cr sample is single phase. On the basis of the crystallographic information file established by the refinement results, the crystal structure of RNSF was constructed by using the VESTA program. The built RNSF crystal model is displayed in Fig. 1d, where the coordination environment surrounding Sc and Na can be clearly observed. Apparently, each Sc or Na is connected with six F to form two kinds of octahedral cages, i.e., $[NaF_6]$ and $[ScF_6]$, in this structural system, while each Rb occupies 12-coordinated cavity to form a regular $[RbF_{12}]$ polyhedron. The three kinds of polyhedral connect with each other into a double perovskite network with $Fm\bar{3}m$ (225) space group of cubic phase. Considering the ionic radius and ionic charge between Na^+ (1.02 Å), Sc^{3+} (0.745 Å) and Cr^{3+} (0.615 Å) with the same coordination number, Cr^{3+} is inclined to substitute the lattice site of Sc^{3+} since the same valence state and the acceptable ionic radius difference.[26] This is also the reason why RNSF:0.03Cr has a shortened lattice parameter and a smaller unit cell volume than those of RNSF host.

The EPR spectrum provided in Fig. S1 of ESI† verifies the valence state of trivalent chromium ion and once again confirms that Cr^{3+} activator has entered RNSF host lattice. The SEM and elemental mapping images shown in Fig. S2 (ESI†) suggest that RNSF:Cr product consists of micro-sized octahedral particulates, in which Cr^{3+} activators are homogeneously dispersed. Fig. 2a presents the calculated electronic structure of RNSF host on the basis of first principles of DFT. Both the
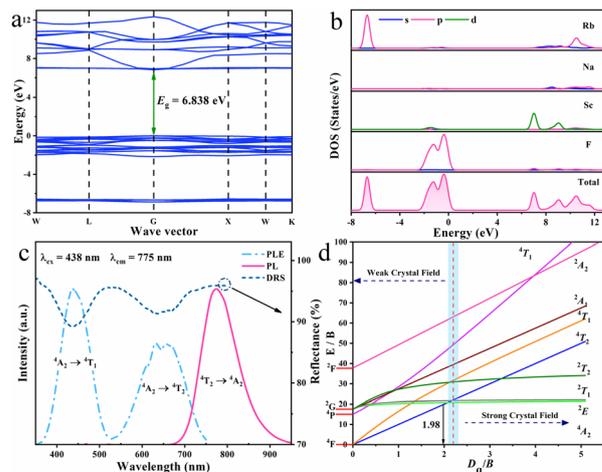
valence band maximum (VBM) and conduction band minimum (CBM) are situated at the G point of Brillouin zone, suggesting the direct bandgap of the host material. The estimated bandgap (6.838 eV) between VBM and CBM is wide enough to accommodate impurity Cr^{3+} energy levels for the generation of Cr^{3+} NIR emission, which contributes to suppressing thermal ionization and thereby achieving high thermal stability.[27,28] The upper part of the VB is dominated by F p orbitals whist the lower part of the CB is composed of Sc d orbitals, illustrating that the luminescent properties of Cr^{3+} in RNSF host highly depend on $[ScF_6]$ octahedral (Fig. 2b).[29]

Fig. 2c gives the PLE, PL, and DR spectra of the RNSF:0.03Cr sample monitored at RT. The PLE spectrum was recorded upon 775 nm light irradiation and consisted of two excitation bands locating at blue and red regions that perfectly fit with the two distinct absorption bands of the DR spectrum, which are originated from the spin-allowed transitions of Cr^{3+} from $^4A_2$ ground state to $^4T_1$ and $^4T_2$ excited states, respectively.[30] Notably, the blue excitation band is much stronger than the red one, suggesting that RNSF:Cr phosphor could be combined with a commercial InGaN chip to assemble a NIR pc-LED device.[31] Additionally, two dips located at 633 and 660 nm are inspected from the $^4A_2 \rightarrow {}^4T_2$ transition, which are associated with Fano antiresonance between weakly coupled $^2E/^2T_1$ and strongly coupled $^4T_2$ levels, as a result, excitation peak reduces and additional peak generates.[32,33] Upon 438 nm light excitation, the PL spectrum exhibits a NIR emission band extending from 650 to 950 nm with peak location at 775 nm and FWHM of 95 nm, which is attributed to Cr^{3+}: $^4T_2 \rightarrow {}^4A_2$ transition in weak coordination environment.[34,35] The NIR emission can be verified by calculating the ratio of Dq/B for the estimation of crystal field strength surrounding Cr^{3+} ion being weak or strong with a dividing point of 2.3. The lower Dq/B ratio means the weaker crystal field strength. In this case, the Dq, B and Dq/B values are calculated to be 1552 cm^{-1}, 782 cm^{-1} and 1.98, respectively, according to the PLE peak energies of $^4T_1$ (22831 cm^{-1}) and $^4T_2$
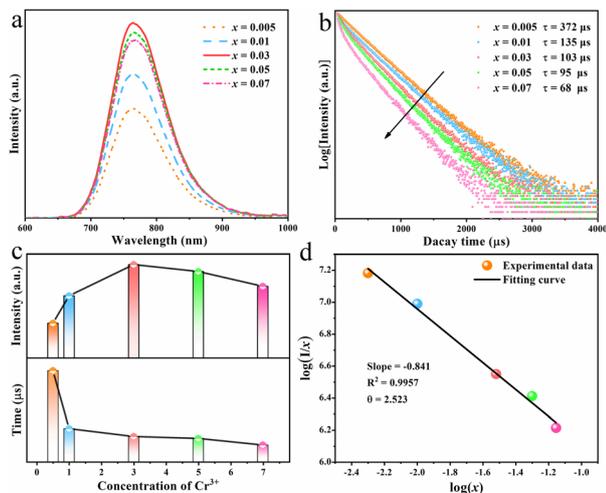
Fig. 3 RNSF:xCr (x = 0.005-0.07) phosphors: (a) concentration-dependent PL spectra upon 438 nm blue light excitation, (b) decay curves, (c) integral PL intensity and lifetime as a function of Cr^{3+} doping content. (d) Fitted result by plotting log (I/x) versus log (x).

Fig. 4 RNSF:0.03Cr phosphor: (a) temperature–dependent PL spectra, (b) relative PL intensity as a function of temperature, (c) and (d) FWHM^2 versus 2kT and fitted curve of ln [(I_0/I_T)−1] versus 1 kT^{-1} based on the modified Arrhenius equation, (e) configurational coordinate diagram.

(15528 cm^{-1}) levels. This result illustrates that Cr^{3+} ions undergo a weak crystal field in RNSF host, resulting in a NIR emission band in this system.[36] The estimation result is marked in the Tanabe-Sugano diagram of Cr^{3+} shown in Fig. 2d. The measured IQE value of RNSF:0.03Cr phosphor is 48.95%, indicating its potential for NIR pc-LED application.

For a deep understanding of the effect of dopant concentration on the luminescent properties of the as-prepared phosphor, the concentration-dependent PL spectra of RNSF:xCr (x = 0.005–0.07) were measured at RT and the results are shown in Fig. 3a. Apparently, the rising Cr^{3+} content (x value) prompts the increase of PL intensity until it reaches x = 0.03, and then causes the declination of PL intensity due to the concentration quenching effect (the upper part of Fig. 3c). Therefore, the optimal x value for RNSF:xCr is determined to be x = 0.03, at which RNSF:0.03Cr has the highest PL intensity and is employed for the subsequent measurements. The corresponding PL decay curves of RNSF:xCr examined at RT are shown in Fig. 3b. All of them abide to a single exponential function, verifying Cr^{3+} ion substitutes the single lattice site of Sc^{3+} in RNSF matrix.[37] Increasing the x value from 0.005 to 0.07, the fitted lifetime descends from 372 to 68 μs (the lower part of Fig. 3c), which is attributable to the intensified non-radiation transition among Cr^{3+} activators.[38] Plotting the relationship between log (I/x) and log (x) on the basis of the Dexter theory, the critical distance between neighbouring Cr^{3+} ions was calculated, which can be used to explain the specific concentration quenching mechanism.[39] In this circumstance, the critical distance R_c is calculated to be 21.66 Å and the θ value is fitted as 2.523, as shown in Fig. 3d, strongly demonstrating that the energy transfer among the nearest or next nearest Cr^{3+} ions is the primary reason for concentration quenching of Cr^{3+} in RNSF host.[40,41]

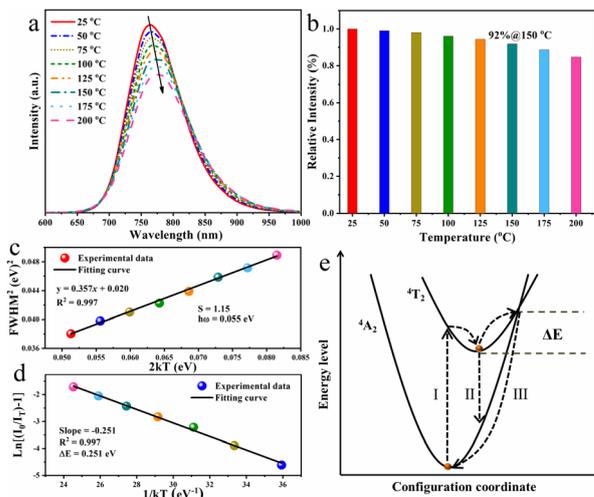The working temperature of LED device may reach 150 °C or even higher because of the accumulated heat during the operation process, resulting in the investigation on the thermal quenching behaviour of the as-obtained RNSF:0.03Cr phosphor is of great importance.[42] Fig. 4a depicts the temperature-dependent PL spectra of RNSF:0.03Cr recorded from 25 to 150 °C, in which the PL intensity diminishes monotonically with the elevated ambient temperatures. When the ambient temperature is increased to 150 °C, the integral PL intensity still preserves 92% of the starting value at 25 °C (Fig. 4b). This ratio is conspicuously higher than a number of Cr^{3+}-activated fluorides (Table S2 in ESI†), indicating the superior anti-thermal quenching performance of the RNSF:0.03Cr NIR phosphor and its potential in NIR pc-LED devices. Moreover, the spectral peak position has a red-shift trend and the corresponding FWHM gradually expands as the temperature increases from 25 to 150 °C. The former phenomenon is attributed to the declined crystal field strength and the intensified non-radiative transitions resulted from lattice expansion at high temperatures, and the latter is always ascribed to the enhanced EPC strength that employs the Huang–Rhys factor (S) as an indicator.[43] The equation of FWHM^2 = 5.57 × S × ($h\omega$)^2 × (1 + 2kT/$h\omega$) can be used to describe the EPC strength by plotting the relationship between FWHM^2 and 2kT, in which hω stands for the phonon energy, and k is the Boltzmann constant.[44] The trustworthy fitting results are shown in Fig. 4c, from which a linear fitting curve with an estimated S value of 1.15 is obtained, demonstrating that the Cr^{3+} activators undergo a low EPC strength in RNSF host to achieve high PL thermal stability.

In order to elucidate the high PL thermal stability of RNSF:Cr phosphor, the activation energy (ΔE) was employed to evaluate the thermal quenching resistance of the titled material by using the modified Arrhenius formula of $I_T = I_0/[1 + A \exp(-\Delta E/k\mathrm{T})]$, where I_0 and I_T represent the integral PL intensities at 25 °C and a given thermodynamic temperature, respectively, k is 8.629 × 10^{-5} eV K^{-1} and A stands for a constant.[45] By plotting ln [(I_0/I_T)−1] versus 1 kT^{-1}, a reliable
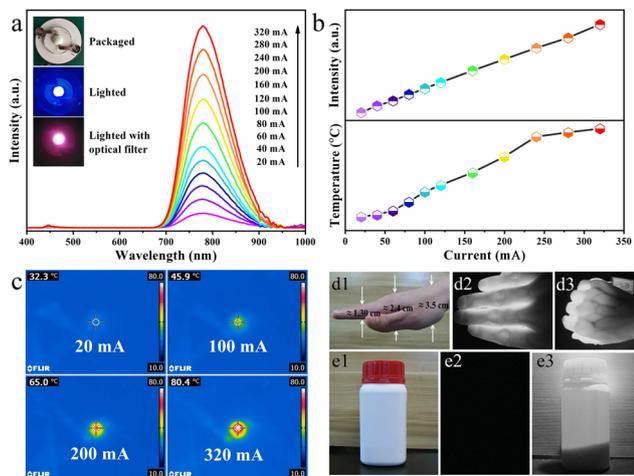
Fig. 5 (a) PL spectra of NIR pc-LED device measured at various driven currents from 20 to 320 mA. (b) Integral PL intensity and temperature of NIR pc-LED device as a function of driven current. (c) Thermographs of LED device captured at 20 mA, 100 mA, 200 mA and 320 mA, respectively. (d) Right hand and photographs of palm and fingers under natural and NIR light illumination using NIR pc-LED as radiation source. (e) Pictures of opaque plastic bottle under natural, dark, and NIR light illumination.

linear fitting curve with a slope of −0.251 is attained, as shown in Fig. 4d, suggesting that the ΔE value is estimated to be 0.251 eV. This value is much larger than RT thermal disturbance energy (0.026 eV), indicating that the energy barrier for non-radiative relaxation is hard to overcome and logically leads to the high thermal stability.[46] The configuration coordinate diagram shown in Fig. 4e can be used to elaborate the thermal quenching behaviour of RNSF:Cr phosphor. Under blue light radiation, electrons of Cr^{3+} can be excited from the low-energy $^4A_2$ state to the high-energy $^4T_2$ level through pathway I. At RT, most of the electrons return to the ground state via pathway II with NIR emission, and the rest of them relax to the ground state in the form of non-radiative transition. At elevated temperatures, the electrons at $^4T_2$ state could be excited to the intersection point of the $^4T_2$ and $^4A_2$ energy levels, and then get back to the ground state via a non-radiative form of way III. The energy barrier between the lowest position and the intersection point is defined as the activation energy (ΔE). Obviously, large ΔE is beneficial for the reduction of non-radiative transition because it is hard to overcome the energy barrier, thus leading to the excellent PL thermal stability.[47] Moreover, The TG curve shown in Fig. S3 (ESI†) further confirms the excellent thermo-chemical stability of RNSF:Cr phosphor, which starts to decompose at a high temperature of 943 °C.

Benefiting from the excellent thermal stability (92%@ 150 °C) and NIR emission of RNSF:0.03Cr phosphor, a NIR pc-LED device was assembled by coating the as-prepared NIR phosphor on a blue InGaN chip. The device photographs and the corresponding PL spectra operated at various driven currents in the range of 20-320 mA are provided in Fig. 5a. It is obvious that the emission spectra are composed of two parts. One is the strong NIR emission assigned to Cr^{3+}:$^4T_2$ → $^4A_2$ transition, and the other is the negligible blue emission

generated by the blue InGaN chip. Obviously, with the increase of driven current, the integral NIR emission intensity shows a continuous increasing trend without light saturation, as shown in the upper part of Fig. 5b, further verifying the excellent PL thermal stability of RNSF:Cr phosphor. Temperature and thermographs of the working LED device under various driven currents captured by a NIR imaging camera are shown in the lower part of Fig. 5b and c, in which the working temperature of the fabricated NIR pc-LED increased from 32.3 °C to 80.4 °C induced by the accumulated heat at higher driven currents. Thus, one can conclude that RNSF:Cr phosphor could be stably used in LED device since its high PL thermal stability. Moreover, as the rising driven current, the NIR output power of the LED device continuously increases and the photoelectric conversion efficiency decreases monotonously (Fig. S4 in ESI†), which are mainly attributable to the decreasing IQE of the blue LED chip at higher temperatures.[48]

In view of the remarkable characteristics of NIR light with non-destruction and penetrability, the manufactured pc-LED device is employed as lighting source for spectroscopy applications of vein imaging and night vision. Considering the absorption of NIR radiation by hemoglobin in human blood, vein imaging analysis was carried out, as shown in Fig. 5d1–3. It turns out that NIR light can easily penetrate ∼1.3 cm thick fingers and ∼2.4 cm thick palm, in which the vein distribution can be clearly observed without any damage to human hand. Moreover, Fig. 5e1–3 exhibit the photographs of opaque reagent bottle that are captured by a camera with natural and NIR modes using the NIR pc-LED as radiation source. Apparently, the photograph of the plastic bottle with white body and red cap is clearly witnessed under natural light illumination, whist nothing is captured without exposure to natural light. However, when the assembled NIR pc-LED device is lighted on, the opaque plastic bottle, as well as the chemical powders inside, are clearly visualized by a NIR camera. These clear demonstration images strongly confirm the potential use of the thermally stable RNSF:Cr phosphor for vein imaging and night vision applications.

Conclusion

In this work, a double perovskite RNSF:Cr fluoride phosphor with blue excitation and NIR emission band was synthesized through a co-precipitation method. The crystal and electronic structures, as well as the luminescent properties were investigated systematically. RNSF:Cr presents a NIR emission band owing to Cr^{3+}:$^4T_2$ → $^4A_2$ spin-allowed transition under blue light excitation, and possesses excellent thermal stability at 150 °C with a retention rate of 92% of that at RT, which is originated from the weak EPC strength (S = 1.15) surrounding Cr^{3+} activators and the large activation energy (ΔE = 0.251 eV) of RNSF:Cr phosphor. By coating RNSF:Cr NIR phosphor on blue InGaN chips, its potential uses in pc-LED devices were explored in different spectroscopy applications.

Author contributions

Conflicts of interest

The authors declare no competing financial interests.

Acknowledgements

References

1 V. Rajendran, M. H. Fang, W. T. Huang, N. Majewska, T. Lesniewski, S. Mahlik, G. Leniec, S. M. Kaczmarek, W. K. Pang, V. K. Peterson, K. M. Lu, H. Chang and R. S. Liu, *J. Am. Chem. Soc.*, 2021, **143**, 19058–19066.

2 Z. Jia, C. Yuan, Y. Liu, X. J. Wang, P. Sun, L. Wang, H. Jiang and J. Jiang, *Light Sci. Appl.*, 2020, **9**, 86–95.

3 M. H. Fang, Z. Bao, W. T. Huang and R. S. Liu, *Chem. Rev.*, 2022, **122**, 11474–11513.

4 J. Zhong, Y. Zhou, F. Du, H. Zhang, W. Zhao and J. Brgoch, *ACS Appl. Mater. Interfaces*, 2021, **13**, 31835–31842.

5 C. Yuan, R. Li, Y. Liu, L. Zhang, J. Zhang, G. Leniec, P. Sun, Z. Liu, Z. Luo, R. Dong and J. Jiang, *Laser Photonics Rev.*, 2021, **15**, 2100227.

6 D. Wen, H. Liu, Y. Guo, Q. Zeng, M. Wu and R. S. Liu, *Angew. Chem., Int. Ed.*, 2022, **134**, e202204411.

7 J. Qiao, S. Zhang, X. Zhou, W. Chen, R. Gautier and Z. Xia, *Adv. Mater.*, 2022, **34**, e2201887.

8 G. Liu, S. Zhang and Z. Xia, *Opt. Lett.*, 2023, **48**, 1296–1299.

9 S. Li, Q. Zhu, X. Li, X. Sun and J. G. Li, *J. Alloys Compd.*, 2020, **827**, 154365.

10 J. Wang, X. Han, Y. Zhou, Z. Wu, D. Liu, C. Zeng, S. Cao and B. Zou, *J. Phys. Chem. Lett.*, 2023, **14**, 1371–1378.

11 N. Ma, W. Li, B. Devakumar, Z. Zhang and X. Huang, *Mater. Today Chem.*, 2021, **21**, 100512.

12 J. Xiang, X. Zhou, X. Zhao, Z. Wu, C. Chen, X. Zhou and C. Guo, *Laser Photonics Rev.*, 2023, **17**, 2200965.

13 X. Zhou, J. Xiang, J. Zheng, X. Zhao, H. Suo and C. Guo, *Mater. Chem. Front.*, 2021, **5**, 4334–4342.

14 Y. Wang, J. Feng, P. Chen, J. Huo, Q. Zhang, S. Liu, M. Tang, J. Li and J. Zhou, *Dalton Trans.*, 2023, **52**, 10071–10078.

15 L. Song, S. Liang, W. Nie, X. He, J. Hu, F. Lin and H. Zhu, *Inorg. Chem.*, 2023, **62**, 11112–11120.

16 J. Xiang, J. Zheng, X. Zhao, X. Zhou, C. Chen, M. Jin and C. Guo, *Mater. Chem. Front.*, 2022, **6**, 440–449.

17 Q. Fan, J. Li, J. Yang, Y. Zhou, Q. Zhou and Z. Wang, *Mater. Res. Bull.*, 2023, **158**, 112065.

18 D. Huang, H. Zhu, Z. Deng, H. Yang, J. Hu, S. Liang, D. Chen, E. Ma and W. Guo, *J. Mater. Chem. C*, 2021, **9**, 164–172.

19 K. Chen, S. Jia, X. Zhang, Z. Shao, Y. Zhou, T. Fan, T. Yu and T. Deng, *Inorg. Chem.*, 2023, **62**, 7964–7975.

20 X. Hu, X. Li, Q. Yang, Y. Ye, Z. Wang, Q. Zhou, H. Tang and Q. Wang, *J. Lumin.*, 2023, **263**, 120095.

21 X. Zhang, K. Chen, T. Deng, J. Yuan, R. Zhou, T. Yu, Y. Zhou and E. Song, *Mater. Today Chem.*, 2022, **26**, 101194.

22 W. Nie, Y. Li, J. Zuo, Y. Kong, W. Zou, G. Chen, J. Peng, F. Du, L. Han and X. Ye, *J. Mater. Chem. C*, 2021, **9**, 15230–15241.

23 F. He, E. Song, Y. Zhou, H. Ming, Z. Chen, J. Wu, P. Shao, X. Yang, Z. Xia and Q. Zhang, *Adv. Funct. Mater.*, 2021, **31**, 2103743.

24 X. Zhang, S. Qing, Y. Qin, Q. Zhou, J. Wan, H. Tang and Z. Wang, *J. Lumin.*, 2023, **254**, 119531.

25 W. Nie, L. Yao, G. Chen, S. Wu, Z. Liao, L. Han and X. Ye, *Dalton Trans.*, 2021, **50**, 8446–8456.

26 S. Qing, X. Zhang, T. Yang, L. Chu, Y. Zhou, J. Wan, Z. Wang, H. Tang and Q. Zhou, *Dalton Trans.*, 2022, **51**, 14214–14220.

27 J. Qiao, J. Zhao, Q. Liu and Z. Xia, *J. Rare Earths*, 2019, **37**, 565–572.

28 H. Zhang, J. Zhong, F. Du, L. Chen, X. Zhang, Z. Mu and W. Zhao, *ACS Appl. Mater. Interfaces*, 2022, **14**, 11663–11671.

29 Y. Yan, M. Shang, S. Huang, Y. Wang, Y. Sun, P. Dang and J. Lin, *ACS Appl. Mater. Interfaces*, 2022, **14**, 8179–8190.

30 J. Lai, W. Shen, J. Qiu, D. Zhou, Z. Long, Y. Yang, K. Zhang, I. Khan and Q. Wang, *J. Am. Ceram. Soc.*, 2020, **103**, 5067–5075.

31 S. Ding, P. Feng, J. Cao, X. Ma and Y. Wang, *ACS Appl. Mater. Interfaces*, 2022, **14**, 44622–44631.

32 A. Lempicki, L. Andrews, S. J. Nettel, B. C. McCollum and E. I. Solomon, *Phys. Rev. Lett.*, 1980, **44**, 1234–1237.

33 O. Taktak, H. Souissi and S. Kammoun, *J. Lumin.*, 2015, **161**, 368–373.

34 S. Liu, H. Cai, S. Zhang, Z. Song, Z. Xia and Q. Liu, *Mater. Chem. Front.*, 2021, **5**, 3841–3849.

35 Y. Zhou, C. Li and Y. Wang, *Adv. Opt. Mater.*, 2022, **10**, 2102246.

36 S. Adachi, *J. Lumin.*, 2021, **232**, 117844.

37 S. Miao, Y. Liang, D. Chen, R. Shi, X. Shan, Y. Zhang, F. Xie and X. J. Wang, *ACS Appl. Mater. Interfaces*, 2022, **14**, 53101–53110.

38 T. Tan, S. Wang, J. Su, W. Yuan, H. Wu, R. Pang, J. Wang, C. Li and H. Zhang, *ACS Sustainable Chem. Eng.*, 2022, **10**, 3839–3850.

39 Y. Chen, F. Liu, Z. Zhang, J. Hong, M. S. Molokeev, I. A. Bobrikov, J. Shi, J. Zhou and M. Wu, *J. Mater. Chem. C*, 2022, **10**, 7049–7057.

40 J. Chen, C. Guo, Z. Yang, T. Li and J. Zhao, *J. Am. Ceram. Soc.*, 2016, **99**, 218–225.

41 L. You, R. Tian, T. Zhou and R. J. Xie, *Chem. Eng. J.*, 2021, **417**, 129224.

42 Q. Song, Z. Liu, H. Jiang, Z. Luo, P. Sun, G. Liu, Y. Liu, H. Jiang and J. Jiang, *J. Am. Ceram. Soc.*, 2021, **104**, 5235–5243.

43 F. Zhao, H. Cai, Z. Song and Q. Liu, *Chem. Mater.*, 2021, **33**, 3621–3630.

44 C. Li and J. Zhong, *Chem. Mater.*, 2022, **34**, 8418–8426.

45 Q. Zhou, L. Dolgov, A. M. Srivastava, L. Zhou, Z. Wang, J. Shi, M. D. Dramićanin, M. G. Brik and M. Wu, *J. Mater. Chem. C*, 2018, **6**, 2652–2671.

46 Y. Wang, Z. Wang, G. Wei, Y. Yang, S. He, J. Li, Y. Shi, R. Li, J. Zhang and P. Li, *Adv. Opt. Mater.*, 2022, **10**, 2200415.

47 Z. Liao, C. Li, J. Zhong, Y. Li and W. Zhao, *Dalton Trans.*, 2023, **52**, 2853–2862.

48 Y. Zhang, Y. Liang, S. Miao, D. Chen, S. Yan and J. Liu, *Inorg. Chem. Front.*, 2021, **8**, 5186–5194.